Lawrence Berkeley National Laboratory

Title
Finite Size Effects on the Real-Space Pair Distribution Function of Nanoparticles

Permalink
https://escholarship.org/uc/item/5z75290p

Author
Gilbert, Benjamin

Publication Date
2009-04-30

Finite Size Effects on the Real-Space Pair Distribution Function of Nanoparticles

Benjamin Gilbert

Earth Science Division, Ernest Orlando Lawrence Berkeley National Laboratory, 1 Cyclotron Road, MS 90R1116, Berkeley, CA 94720, USA. E-mail: bgilbert@lbl.gov

Synopsis   [Click here to enter Synopsis]

Abstract   The pair distribution function (PDF) method is a powerful approach for the analysis of the structure of nanoparticles. An important approximation used in nanoparticle PDF simulations is the incorporation of a form factor describing nanoparticle size and shape. The precise effect of the form factor on the PDF is determined by both particle shape and structure if these characteristics are both anisotropic and correlated. The correct incorporation of finite size effects is important for distinguishing and quantifying the structural consequences of small particle size in nanomaterials.

Keywords: pair distribution function; nanoparticle; disorder

1. Introduction

There is considerable current interest in the study of inorganic nanoparticles that exhibit novel size-dependent electronic, chemical and optical properties. The threshold below which finite size effects are discernable in nanomaterial properties is generally very small (typically < 10 nm), and materials of such small dimensions can also exhibit structural modification due to the large fraction of atomic sites close to surface. Full understanding of the interrelationships between size, structure and electronic properties remains an outstanding problem for many nanomaterials because there is no ideal method for the structural analysis of nanoparticles (Billinge & Levin, 2007). High-resolution transmission electron microscopy (HRTEM) is an important approach for revealing the shape and structure of individual nanoparticles, but is relatively insensitive to disorder and surface structure. Powder diffraction measurements of nanoparticle structure are subject to substantial size-related peak broadening and overlap, as well as systematic errors associated with Bragg peak analysis of small crystallites (Palosz et al., 2002). Using methods developed in the protein crystallography field, a few examples of highly-monodisperse cluster compounds and nanoparticles have been successfully assembled into oriented crystalline arrays, permitting the atomic positions of both nanoparticles and ligands to be refined (Soloviev et al.,

2001; Jadinsky et al., 2007). However, the vast majority of nanomaterials are unlikely ever to be analyzed in this manner. Phase retrieval methods may permit atomic-scale three-dimensional (3D) reconstruction of the structures of single nanoparticles analyzed by fully coherent electron or x-ray scattering (Miao et al, 2001). However, the currently attainable spatial resolution is at least an order of magnitude away from this goal, and many technological challenges remain.

The atomic pair distribution function (PDF) is a description of real-space structure that is less complete than full 3D atomic structure, but is experimentally attainable and proving to be of great value for the study of nanoparticles. PDF analysis has been performed for many years (e.g., Posner et al., 1980), but is increasingly adopted for structural analysis because synchrotron x-ray sources and neutron sources now permit data acquisition with high accuracy up to large values of the momentum transfer, $q = 4\pi \sin\theta / \lambda$, where 2θ is the scattering angle and λ is the x-ray wavelength. The PDF method is versatile (it can be applied to any material) and is a particularly valuable complement to conventional diffraction for the studies of amorphous materials (Sampath et al., 2003) and crystalline materials that exhibit short-range structural modifications (Petkov et al., 1999). As described below, the PDF of periodic (unit cell based) or non-periodic (cluster) structural models is straightforward to calculate. Thus, PDF data may serve as an input to reverse Monte Carlo (RMC) codes that seek (non-unique) structural solutions most compatible with the experimental data (Proffen & Neder, 1997). Moreover, refining crystal structure against real-space data is a powerful approach for determining unit cell parameters and detecting and quantifying disorder.

There have been numerous applications of PDF analysis to the structure of nanomaterials for determining crystal phase, unit cell parameters, and quantifying various types of disorder or defect structure (Petkov et al., 2002; Gateshki et al., 2004; Petkov et al., 2004; Gilbert et al., 2004; Masedeh et al., 2007; Pradhan et al., 2007). In particular, studies of ferrihydrite and mackinawite, natural iron-bearing nanomaterials, demonstrate that many materials that appear to be "x-ray amorphous" are in fact better described as aggregates of very small crystallites (Wolthers et al., 2003; Michel et al., 2005; Michel et al., 2007). By basing nanoparticle PDF analysis upon the crystallographic unit cell, these studies implicitly assume the nanomaterials to be homogeneous, with any size-dependent structural modifications evenly distributed throughout each particle. The validity of this assumption appears to be strongly material dependent. For example, while evidence of strongly disordered surface region has been found in mercaptoethanol-coated ZnS nanoparticles synthesized in room temperature aqueous solution (Gilbert et al., 2004) as well as ZnS nanoparticles synthesized by alternative methods (Gilbert et

al., 2006), triocytl phosphine oxide (TOPO) coated CdSe nanoparticles synthesized at 300˚C did not show evidence of any substantial surface disorder (Masedeh et al., 2007).

Given the growth of computational power, an obvious question is whether the structure of an entire cluster or nanoparticle can be understood, or even refined, with no assumption of atomic-scale periodic symmetry. Dispensing with assumptions of periodicity permits the most exciting avenue for connecting experiment with structure simulation and visualization. Molecular dynamics simulations provide a powerful approach for predicting structure that can be evaluated by comparing predicted and experimental PDF data (Wright, 1993; Zhang et al., 2003). Moreover, an exciting recent development is the demonstration that a novel PDF analysis method is capable of solving the complete structure of the C_{60} molecule without prior assumptions (Juhás et al., 2006). Nevertheless, there are extreme challenges associated with determining the positions of hundreds of atoms in a model nanoparticle. Thus, the purpose of this contribution is to summarize the pure size dependent effects on nanoparticle PDF data so that they may be distinguished from structural effects and properly incorporated into PDF analysis approaches.

Numerous authors have derived and incorporated spherical particle form factors into descriptions of diffraction and PDF data. However, many nanomaterials are non-spherical and possess, for example, spheroidal (Efros & Rodina, 1993; Shiang et al., 1995), rod-like (Manna et al., 2000; Puntes et al., 2001) or sheet-like morphologies (Chen et al., 1996; Lin et al., 2006). Although the investigation of particle morphology from XRD data is routine (Popa, 1998), the incorporation of anisotropic shape effects into PDF analysis is rare. While the present contribution does not provide a complete summary of form factors for common nanomaterial morphologies, it describes one method for their calculation with explicit results for prolate and oblate spheroids. We first provide a brief introduction to the PDF technique.

2. Theory and Simulation

The goal of a PDF experiment is the measurement of the scattering intensity, $I(q)$, and the treatment of this quantity to obtain the sample structure factor, $S(q)$, the component of the data that is related to the relative arrangement of scattering objects (atoms) in space. The acquisition, treatment and correction of experimental scattering data to obtain the structure factor require several non-trivial precautions, as described elsewhere (Thijsse, 1984; Toby & Egami, 1992). The value of the structure factor is that it is related to a statistical description of the atomic positions in the sample called the pair correlation function, $\rho(\mathbf{r})$ (defined in **Appendix A**). For a single scattering object,

$$S(\mathbf{q}) - 1 = \int [\rho(\mathbf{r}) - \rho_o] e^{-i\mathbf{q}\cdot\mathbf{r}} d^3\mathbf{r} \qquad (1)$$

In an ideal powder diffraction experiment, individual grains are present in all orientations with respect to the x-ray beam. In this sense, the sample is statistically isotropic (even if individual grains are anisotropic), and the full PCF may be replaced by its angular average, $\overline{\rho(\mathbf{r})}$, where

$$\overline{\rho(\mathbf{r})} = \int\limits_{\theta=0}^{\pi} \int\limits_{\varphi=0}^{2\pi} \rho(r,\theta,\varphi) \sin\theta d\theta \frac{d\varphi}{2\pi}. \qquad (2)$$

Here, we use the overbar to indicate the angular average, to distinguish between this and a function that is intrinsically isotropic, denoted $\rho(r)$. This distinction is useful because in general $\overline{f(\mathbf{r})\rho(\mathbf{r})} \neq \overline{f(\mathbf{r})}\,\overline{\rho(\mathbf{r})}$. Using the substitution $\mathbf{q}\cdot\mathbf{r} = qr\cos\theta$, integration of **Eqn 1** then gives one of the fundamental equations of PDF analysis:

$$q[S(q) - 1] = \int G(r)\sin(qr)dr, \qquad (3)$$

where the pair distribution function, $G(r) = 4\pi r\left[\overline{\rho(\mathbf{r})} - \rho_o\right]$. This relationship shows that the PDF provides only the r-dependent structure that is different from the mean atom density, ρ_o. Applying the inverse transform,

$$G(r) = \frac{2}{\pi} \int q[S(q) - 1]\sin(qr)dq. \qquad (4)$$

2.1. Simulating the PDF of ideal infinite samples

The simulation of PDF patterns is computationally tractable because the principal task is the conversion of a candidate structure (either a unit cell or an atomic coordinate representation) to a list of interatomic distances (Marciniak et al., 1996). This structural information may be compared to experimental data using the following expression (Wright, 1988; Proffen & Billinge, 1999):

$$G(r) = \{\frac{1}{r}\sum_i\sum_j \frac{f_i f_j}{\langle f\rangle^2}\Gamma(r - r_{ij}, \sigma_{vib}, \sigma_{fin}) - 4\pi r\rho_o\}\exp[-r^2\omega_Q^2/2], \qquad (5)$$

where $\Gamma(r - r_{ij}, \sigma_{vib}, \sigma_{fin})$ is a correlation peak representing the contribution from a single interatomic distance between atoms i and j that is broadened due by thermal vibrations of the atoms and by the finite Q-range of the data. Each contribution is weighted by the pair of atomic scattering strengths appropriate to the measurement technique (neutron or x-ray scattering). In this contribution, $f_i(Q)$ is the atomic form factor for x-ray scattering. To an accuracy of 1-2%,

the Q-dependence of the x-ray form factor may be neglected and f_i substituted by the atomic number.

An important consideration for the comparison of experimental and simulated PDF is that finite data range affects the profile of each peak in the experimental PDF and can additionally lead to the presence of termination ripples (Wright, 1988). Finite data effects can be explicitly incorporated in the simulated $G(r)$ (Chung & Thorpe, 1997). Alternatively, multiplying the experimental Q-weighted structure factor by a Gaussian window function before transformation suppresses termination ripples, and the finite-data and Debye-Waller-type disorder contributions to simulated PDF peak width can be combined in quadrature to a final total width,

$$\sigma_{tot}^2(r) = \sigma_{vib}^2(r) + \sigma_{fin}^2 + \sigma_{win}^2 \tag{6}$$

Because the thermal motion of nearby atoms is not independent, the vibrational contribution to PDF peak width broadening is less for nearby atoms than for distant atoms whose motions are entirely uncorrelated. This effect may be included in $\sigma_{vib}^2(r)$ by an empirical factor proportional to r^{-1} (Proffen & Billinge, 1999) or by a theoretical method (Jeong et al., 1999).

Both the finite energy resolution of the x-ray or neutron source and the finite angular resolution of the detector contribute a broad envelope function that causes the PDF to decay at large interatomic distance. This function is approximated by a Gaussian envelope, characterized by ω_Q and centred at $r = 0$ (Toby & Egami, 1992). Material and experiment dependent parameters such as ω_Q may be obtained from a fit to experimental data from a highly crystalline standard, as shown in **Figure 1**. Proper analysis of nanoparticle data requires that the experimental limitations first be quantified in this way for the particular experimental geometry. This is particularly true for two dimensional (2D) image plate x-ray detectors, which provide exceptionally fast data acquisition at the expense of angular resolution (Chupas et al., 2003). The real-space range accessible with 2D detectors is correspondingly shorter than with scanning detectors.

2.2. PDF from homogeneous finite samples

Modern measurements permit the acquisition of accurate PDF data up to several hundreds of Ångstroms in interatomic distance (e.g., Chung et al., 2005). Thus, in many kinds of nanoscale samples that can be routinely synthesized, finite specimen size may be the dominant cause for the apparent truncation of the PDF with increasing interatomic distance. The simplest treatment of the finite size effect is achieved by assuming that the material is homogeneous (the distribution of atoms around one of them is independent of the choice of atom) and that this property is

unaffected by the small particle size (Guinier, 1963). These assumptions neglect the possibility of surface relaxation, but permit the PCF to be factorized into $\rho_\infty(\mathbf{r})$, which describes an infinite material, and a shape factor $f(\mathbf{r})$, which incorporates the finite size and shape information. As derived in **Appendix A**, the modified structure factor is:

$$S(\mathbf{q}) - 1 = \int f(\mathbf{r})[\rho_\infty(\mathbf{r}) - \rho_o]e^{-i\mathbf{q}\cdot\mathbf{r}}d^3\mathbf{r} \tag{7}$$

For isotropic (powder) samples, the observed diffraction intensity is a function only of the magnitude of the momentum vector. Consequently, we can write the integral as a sine transform of the angular average of the integrand (denoted by an overbar; c.f. **Eqn. (2)**):

$$q\big[S(q) - 1\big] = \int \overline{4\pi r f(\mathbf{r})[\rho_\infty(\mathbf{r}) - \rho_o]}\sin(qr)dr \tag{8}$$

The integrand is a product of two functions that, if they are both anisotropic, may exhibit *correlated angular dependencies*. The function $f(\mathbf{r})$ is isotropic for spherical particles, while $\rho_\infty(\mathbf{r})$ is isotropic for amorphous or *cubic* materials. If one or both functions are isotropic, the immediate result is that the PDF of a finite material is equivalent to the bulk PDF truncated by the real-space shape factor:

$$G(r) = f(r)G_\infty(r) \tag{9}$$

By contrast, if both the particle shape and interior structure are anisotropic,

$$G(r) = \overline{4\pi r f(\mathbf{r})\big[\rho_\infty(\mathbf{r}) - \rho_o\big]} \tag{10}$$

2.2.1. Calculation of $f(\mathbf{r})$

Guinier (1963) showed that the shape factor, $f(\mathbf{r})$, is equal to the fractional volume common to two identical overlapping bodies displaced by $\mathbf{r}(r,\theta,\phi)$. Thus, the finite size effect can be expressed as $f(r,\theta,\phi) = V'(r,\theta,\phi)/V$, where V' is the common volume shared by two objects of volume V. V' is shown graphically for a spheroidal particle in **Figure 2**, a case treated in detail in **Appendix B**.

2.2.2. Calculation of $\overline{f(\mathbf{r})}$

An explicit expression for the angular average of the shape factor, $\overline{f(\mathbf{r})}$, is required not only when the material structure is anisotropic, but for all materials to correctly account for the finite size effect on the amorphous background. Direct calculation of $\overline{f(\mathbf{r})}$ as a geometric modification of $G(r)$ for materials with an isotropic crystal or amorphous structure can be performed for

6

certain particle shapes (M. F. Thorpe, 2004), and this is equivalent to Guinier's approach. Here we consider only shapes with an axis of rotational symmetry, and thus

$$\overline{f(\mathbf{r})} = \frac{1}{V}\int \sin\theta V'(r,\theta)d\theta. \tag{9}$$

This approach is used to derive the results given below.

Sphere. The result for a sphere of diameter D and interatomic distance r is given by several authors (Guinier, 1963; Azaroff, 1968), and is repeated here.

$$f_{sphere}(r,D) = 1 - \frac{3}{2}\left(\frac{r}{D}\right) + \frac{1}{2}\left(\frac{r}{D}\right)^3. \tag{10}$$

Spheroid. A spheroid is an ellipsoid with two equal axes, denoted a and c, with c parallel to the z-axis. TEM observations have shown that CdSe nanoparticles with the wurtzite structure frequently form prolate spheroids rather than spheres (Efros & Rodina, 1993; Shiang et al., 1995). For implementation in PDF simulations it is convenient to describe a spheroid by the radius, R, of a sphere with an identical volume, and its ellipticity, e, defined by

$$e \equiv \sqrt{1 - \frac{a^2}{c^2}} \quad \text{for prolate spheroids } (c > a) \tag{11}$$

$$e \equiv \sqrt{1 - \frac{c^2}{a^2}} \quad \text{for oblate spheroids } (c < a). \tag{12}$$

The derivation of the shape factors for prolate and oblate spheroids is given in **Appendix B**. Here we state the result in a form that emphasizes its similarity with the spherical shape factor.

$$f_{spheroid}(r,D) = 1 - \left(\frac{3}{2}\right)\left(\frac{r}{\sqrt{\eta}D}\right)\Gamma_1(e) + \left(\frac{1}{2}\right)\left(\frac{r}{\sqrt{\eta}D}\right)^3\Gamma_2(e) \tag{13}$$

The exact expressions for $\Gamma_1(e)$ and $\Gamma_2(e)$ are different for oblate and prolate spheroids. They and the term η approach unity as the ellipticity approaches zero. Due to the constraint of fixed volume, this expression for prolate spheroid is not a suitable approximation for long cylindrical rods.

2.2.3. Non-cubic materials

If both the shape and structure are anisotropic, a simple factorization of the PDF (i.e., **Eqn. 9**) is not possible. This is because the crystal lattice will be consistently oriented with respect to the symmetry axes of a non-spherical particle and the shape factor has a dependence on this orientation. Hence,

$$G(r) = 4\pi r \left[\overline{f(\mathbf{r})\rho_\infty(\mathbf{r})} - \overline{f(\mathbf{r})}\rho_o \right] \tag{14}$$

In these circumstances, the PDF cannot be simulated by combining separate calculations of $\overline{f(\mathbf{r})}$ and $\overline{\rho_\infty(\mathbf{r})}$. Rather, the scaling factor $f(r,\theta,\varphi)$ due to finite size must be applied for each interatomic distance individually when employing **Eqn. 14**, to account for the orientation of the interatomic vector $\mathbf{r}_{ij}$ relative to the anisotropic nanoparticle shape. Large differences in the intensities of particular PDF peaks can result. **Figure 4** compares simulated PDFs for *hexagonal* wurtzite ZnS as prolate spheroid nanoparticles for two orientations of the crystallographic axes relative to the rotational axis of the spheroid. To my knowledge, the observation of correlated crystallographic and morphological effects on PDF peak intensities has not been reported for any real nanomaterial. However, the chemical factors that lead to anisotropic nanoparticle shapes are generally highly associated with crystallographic direction through mechanisms such as preferential growth directions or selective surface adsorption, and thus detectable effects in PDF data would be expected.

2.2.4. Distribution of particle sizes

With the exception of certain inorganic cluster compounds any nanoparticle synthesis produces a range of particle sizes. No attempt is made here to derive analytical expressions for the shape factors given above to incorporate a specific distribution of sizes (e.g., Gaussian or log-normal distributions). However, the effect of size polydispersity may be included numerically, and examples are given in **Fig. 3c**.

3. Fitting the PDF of nanoparticles

3.1. Fitting particle size and shape

It has been speculated that nanoparticle size can be directly determined during fits to PDF data because the *r*-dependent truncation of the PDF is such a clear effect. However, while some studies that have compared particle size estimated from PDF data with size determined using independent methods have obtained good agreement (Masedeh et al., 2007; Michel et al., 2007), others have found the PDF-derived size to be a significant underestimate (Gilbert et al., 2004; Pradahn et al., 2007). As is the case for conventional powder diffraction, the effects of structural disorder and particle size on PDF data are highly correlated, and it is risky to fit particle size to PDF data without certainty that the nanoparticle is highly crystalline. Moreover, it is unclear whether PDF fitting that includes additional size and morphology parameters can be implemented in stable, efficient code. Hence the use of independent methods to obtain particle size and shape,

such as small-angle x-ray scattering (SAXS) or TEM is highly recommended. Only if particle size and shape are known accurately can structural modifications be unambiguously detected from the PDF.

3.2. Fitting structural modifications

We briefly illustrate the use of nanoparticle form factors in the analysis of nanoparticle structure with PDF.

3.2.1. Simple structure fitting

Ceria (CeO_2) nanoparticles can exhibit a lattice expansion associated with the partial substitution of Ce^{3+} for Ce^{4+} in the fluorite structure (Tsunekawa et al., 2000). We use PDF analysis to confirm the structure of CeO_2 nanoparticles synthesized by the method of Zhang et al., (2004) and to test for lattice expansion. Experimental and material parameters were first refined against PDF data from bulk CeO_2 and held constant when fitting the nanoparticle data, to which size, shape, additional harmonic disorder and isotropic lattice expansion parameters were fitted. As the particle size and shape were not well constrained from TEM imaging of this sample, a prolate spheroid shape factor was freely varied during the fit. This shape factor provided a better fit of the truncation envelope of the nanoparticle PDF than either a spherical shape factor or the finite resolution function (the exponential factor in **Eqn. 5**). The best fit is given in **Fig. 5**, which shows that the nanoparticles maintain the fluorite structure of bulk ceria. Imperfect agreement with the intensities of the low-r peaks is an indication of correlated thermal disorder that is poorly accounted for by the empirical method. Similar discrepancies, in fact, are observed in fits to the bulk data (not shown). Despite the small particle size (~ 2 nm diameter), a relatively small lattice expansion of 0.12 % was obtained, indicating that the synthesis method produces highly pure Ce^{4+} ceria nanoparticles. PDF refinement has been used to detect interstitial oxygen defects in CeO_2 nanopowder (Mamontov & Egami, 2000), but a similar analysis is not attempted here.

3.2.2. Short-range order fitting

We have observed that ZnS nanoparticles can contain significant internal strain that causes a more rapid truncation of the PDF than would be expected from small particle size alone. By independently characterizing finite-size contributions to the PDF truncation function, the strain contribution may be isolated. **Figure 6** shows an example of this approach. ZnS nanoparticles prepared by a precipitation reaction in methanol exhibit a highly disordered structure based on the *cubic* sphalerite phase that can be substantially ordered by water adsorption (Zhang et al., 2003)

or tight aggregation during slow drying (Huang et al., 2004). Ultraviolet – visible (UV-vis) absorption spectroscopy and TEM analysis indicate a particle diameter that is close to 3 nm and a nearly spherical morphology. In **Figure 6**, we fit the PDF of such ZnS nanoparticles that have been crystallized through aggregation. The fit is performed by taking experimental and thermal parameters from a fit to bulk *cubic* ZnS (**Figure 1**) and additionally applying the shape factor for a 3 nm diameter sphere.

Due to the presence of strain in the ZnS nanoparticles, incorporation of the shape factor does not fully account for the truncation of PDF intensity. Two additional quantitative trends must be included to achieve a reasonable fit. The first is a static disorder contribution to PDF peak broadening, $\sigma^2_{static}(r)$. For simplicity, the *r*-dependence of this term is assumed to be the same as for correlated thermal disorder (but with different constant factor). The presence of additional structural disorder in nanoparticles relative to bulk crystals is well established from EXAS analyses (Rockenburger et al., 1998). Second, as previously observed in fits to the PDF data from mercaptoethanol-coated ZnS nanoparticles (Gilbert et al., 2004), an additional short-range order (SRO) scaling factor that is a function of interatomic distance is required to obtain a good fit between experimental and simulated PDFs. All contributions to PDF peak widths and intensities are given in **Figure 6c & d**.

The requirement for a SRO factor is interpreted to indicate the present of a complex strain field throughout the nanoparticle interior. At greater interatomic distances within the nanoparticle, the equilibrium positions of atoms lie farther from the positions predicted by translating the input unit cell, and this causes a faster loss of PDF peak intensity with increasing *r* than expected by morphological factors. Clearly, however, the need to include this term highlights that there are important aspects of ZnS nanoparticle structure that are omitted by the underlying model. Specifically, the assumption that the environment of every atom can be estimated by the structure of the bulk material plus strain and disorder (i.e., a single unit cell approach) is inadequate for materials in which there is diversity in local structure among the atomic sites. Nevertheless, quantitative fitting procedures can serve to test and refine structural models until numerical modelling methods have the capacity and accuracy to handle whole-nanoparticle calculations.

4. Conclusions and Outlook

PDF analysis of inorganic nanoparticles reveals the presence of structural modifications that are difficult to discern from direct imaging in the transmission electron microscope or from conventional powder diffraction. Furthermore, the use of high-energy x-ray scattering permits *in*

situ studies that can reveal dynamic aspects of nanoparticle structure. The PDF is easy to simulate, facilitating structural studies, and the examples presented here show that modifications in nanoparticle structure relative to bulk materials can be quantified with simple models that neglect diversity of atomic sites within nanoparticles. The discrepancies between simple model analysis and the experimental data emphasize the need to develop computationally more powerful full-nanoparticle simulation methods. Furthermore, the use of more sophisticated descriptions of correlated thermal motion will improve the accuracy with which the PDF of structural models can be simulated.

References

Azaroff, L. V. *Elements of X-Ray Crystallography.* McGraw-Hill, 1968.

Billinge, S. J. L & Thorpe, M. F. (Eds.). *Local Structure from Diffraction.* Plenum Press, New York, 1998.

Billinge, S. J. L & Levin, I. (2007) *Science* **316**, 561

Chen, R., Zavalij, P. Z. & Whittingham M. S. (1996) *Chem. Mater.* **8**, 1275

Chung, J. S. & Thorpe, M. F. (1997) *Phys. Rev. B* **55**, 1545-1553.

Chung, J. H., Proffen, Th., Shamoto, S., Ghorayeb, A. M., Croguennec, L., Tian, W., Sales, B. C., Jin, R., Mandras, D. & Egami, T. (2005) *Phys. Rev. B* **71**, 064410.

Chupas, P. J., Qiu, X., Hanson, J. C., Lee, P. L., Grey, C. P. & Billinge, S. J. L. (2003) *J. Appl. Cryst.* **36**, 1342-1347.

Dash, R. K., Voyles, P. M., Gibson, J. M., Treacy, M. M. J., Keblinski, P. (2003) *J. Phys. Condens. Matt.* **15**, S2425-2435.

Efros, A. L. & Rodina, A. V. (1993) *Phys. Rev. B* **47**, 10005.

Gateshki, M., Hwang, S.-J., Park, D. H., Ren, Y. & Petkov, V. (2004) *J. Phys. Chem. B* **108**, 14956-14963.

Gilbert, B., Huang, F., Lin, Z., Goodell, C., Zhang, H. & Banfield, J. F. (2006) *Nanoletters,* **6**, 605-610.

Gilbert, B., Huang, F., Zhang, H., Waychunas, G. A. & Banfield, J. F. (2004) *Science* **305**, 651-654.

Glatter, O. (1979) *J. Appl. Cryst.* **12**, 166-175.

Glatter, O. (1991) in Lidner, P. & Zemb, Th. (eds) *Neutron, X-Ray and Light Scattering.* Amsterdam: Elsevier.

Guinier, A. (1963) *X-ray diffraction in crystals, imperfect crystals and amorphous bodies*. W.H. Freeman & Co., San Francisco.

Huang, F., Gilbert, B., Zhang, H. & Banfield, J. F. (2004) *Phys. Rev. Lett.* **92**, 15501.

Jadzinsky, P.D., Calero, G., Ackerson, C. J., Bushnell, D. A. & Kornberg, R. D. (2007) *Science* **318**, 430.

Jeong, I.-K., Proffen, Th., Mohiuddin-Jacobs, F. & Billinge, S. J. L. (1999) *J. Phys. Chem. A* **103**, 921-924.

Lin, Z., Gilbert, B., Liu, Q. and Huang, F. (2006) J. *Am. Chem. Soc.* **128**, 6126.

Mamontov, E. & Egami, T (2000) *J. Phys. Chem. Solids* **61**, 1345-1356.

Manna, L., Scher, E. C. & Alivisatos, A. P. (2000) *J. Am. Chem. Soc.* **122**, 12700-12706.

Marciniak, H., Gierlotka, S. & Palosz, B. (1996) *Mater. Sci. Forum.*, **228-231**, 39-42.

Miao, J., Hodgson, K. O., & Sayre, D. (2001) *Proc. Nat. Sci. Acad. USA* **98**, 6641.

Michel, F. M., Antao, S. M., Chupas, P. J., Lee, P.L., Parise, J. B. & Schoonen, M. A. A. (2005) *Chem. Mater.* **17**, 6246

Michel, F. M., Ehm, L., Antao, S. M., Lee, P. L, Chupas, P. J., Liu, G., Strongin, D. R., Schoonen, M. A. A., Phillips, B. L. & Parise, J. B. (2007) *Science* **316**, 1726.

Palosz, B., Grzanka, E., Gierlotka, S., Stel'Makh, S., Pielaszek, R., Bismayer, U., Neuefeind, J., Weber, H.-P. & Palosz, W. (2002) *Acta Physica Polonica (A)* **102**, 57-82.

Pokrant, S. & Whaley, K. B. (1999) *European J. Phys*. **6**, 255-267.

Petkov, V., Jeong, I.-K., Chung, J. S., Thorpe, M. F., Kycia, S. & Billinge, S. J. L. *Phys. Rev. Lett.* (1999) **83**, 4089-4092.

Petkov, V., Billinge, S. J. L., Larson, P., Mahanti, S. D., Vogt, T., Rangan, K. K. & Kanatzidis, M. G. (2002) *Phys. Rev. B* **65**, 092105.

Petkov, V., Zavalij, P. Y., Lutta, S., Whittingham, M. S., Parvanov, V. & Shastri, S. (2004) *Phys. Rev. B* **69**, 085410.

Popa, N. C. (1998) *J. Appl. Phys.* **25**, 611.

Posner, A. S., Betts, F. & Blumenthal, N. C. (1980) *Prog. Crystal Growth Charact*. **3**, 49-64.

Pradhan, S. K., Deng, Z. T., Tang, F., Wang, C., Ren, Y., Moeck, P. & Petkov, V. (2007) *J. Appl. Phys.* **102**, 044304.

Proffen, Th. & Neder R. B. (1997) *J. Appl. Cryst.* **30**, 171-175.

Proffen, Th. & Billinge, S. J. L. (1999) *J. Appl. Cryst.* **32**, 572-575.

Proffen, Th., Petkov, V., Billinge, S. J. L. & Vogt, T. (2002) *Z. Krystallogr.* **217**, 47-50.

Puntes, V. F., Krishnan, K. M. & Alivisatos, A. P. (2001) *Science* **291**, 2115-2117.

Puzder, A., Williamson, A. J., Gygi, F. & Galli, G. (2004) *Phys. Rev. Lett.* **92**, 217401.

Rockenburger, J., Troger, L., Tisher, M., Grundmann, M., Eychmuller, A. & Weller, H. (1998) *J. Chem. Phys*. **108**, 7807-7815.

Sampath, S., Benmore, C. J., Lantzky, K. M., Neuefeind, J., Leinenweber, K., Price, D. L. & Yarger, J. L. (2003) *Phys. Rev. Lett.* **90**, 115502.

Shiang, J. J., Kadavanich, A. V., Grubbs, R. K. & Alivisatos, A. P. (1995) *J. Phys. Chem.* **99**, 17417-17422.

Soloviev, V. N., Eichhöfer, A., Fenske, D. & Banin, U. (2001) *J. Am. Chem. Soc.* 123, 2354-2364.

Thijsse, B. (1984) *J. Appl. Cryst.* **17**, 61-76.

Thorpe M. F. (2004) personal communication.

Toby, B. H & Egami, T. (1992) *Acta Cryst.* **A48**, 336-346.

Tsunekawa, S., Ishikawa, K., Li, Z. Q., Kawazoe, Y. & Kasuya, A. (2000) *Phys. Rev. Lett.* **85**, 3440-3443.

Wolthers, M,. van der Gaast, S. J., & Rickard, D. (2003) *Am. Mineral.* **88**, 2007

Wright, A. C., Hulme, R. A., Grimley, D. I., Sinclair, R. N., Martin, S. W., Price, D. L. & Galeener, F. L. (1991) *J. Non-Cryst. Solids* **129**, 213.

Wright, A. C. (1988) *J. Non-Cryst. Solids* **106**, 1.

Wright, A. C. (1993) *J. Non-Cryst. Solids* **159**, 264-268.

Wright, A. C., Hulme, R. A., Grimley, D. I., Sinclair, R. N., Martin, S. W., Price, D. L. & Galeener, F. L. (1991) *J. Non-Cryst. Solids* **129**, 213.

Zhang, H., Gilbert, B., Huang F. & Banfield, J. F. (2003) *Nature* **424**, 1025-1029.

Zhang, F., Jin, Q. & Chan, S.-W. (2004) *J. Appl. Phys.* **95**, 4319-4326.

Appendix A. The finite size effect on *S(q)* and *G(r)*

We show how the finite particle size can be incorporated into the definition of the structure factor with the use of a particle form factor (Guinier, 1963). It is assumed that the sample consists of very small particles, each of the same size and shape, and with statistically equivalent arrangements of interior atoms.

A1. Descriptions of the atomic positions in a powder sample

In single particle of volume, *V*, the positions of *N* identical atoms are given by the atomic density function,

$$p(\mathbf{r}) = \sum_i \delta(\mathbf{r} - \mathbf{r}_i). \tag{A1}$$

This complete description cannot be accessed by a powder scattering experiment. However, for a material that is *homogeneous*, the distribution of atoms in the vicinity of a single atom is independent of the choice of atom or particle. Thus, a statistical description of such a material, independent of the location of the origin, is given by the density-density correlation function, $c(\mathbf{r})$, which is the probability per unit volume of finding an atom at position $\mathbf{r}$ from any chosen atom. The closely related pair correlation function (PCF), $\rho(\mathbf{r})$, describes the probability that a

finite vector $\mathbf{r}$ joins two different atoms. These functions differ only by the delta function that represents the central atom always included in the definition of $c(\mathbf{r})$:

$$c(\mathbf{r}) = \rho(\mathbf{r}) + \delta(\mathbf{r}). \tag{A2}$$

A2. The structure factor for infinite samples

For homogeneous materials, the structure factor is given by the Fourier transform of the density-density correlation function.

$$S(\mathbf{q}) = \int c(\mathbf{r})e^{-i\mathbf{q}\cdot\mathbf{r}}d^3\mathbf{r} \tag{A3}$$

Applying Eqn. (15), and making the substitution $\rho(\mathbf{r}) = \rho_o + [\rho(\mathbf{r}) - \rho_o]$, where ρ_o is the mean atom number density, gives:

$$S(\mathbf{q}) = \int \left(\rho_o + \delta(\mathbf{r}) + [\rho_\infty(\mathbf{r}) - \rho_o]\right)e^{-i\mathbf{q}\cdot\mathbf{r}}d^3\mathbf{r}. \tag{A4}$$

The first term describes the small-angle scattering contribution, which may be neglected for PDF analysis. Using $\int \delta(\mathbf{r})e^{-i\mathbf{q}\cdot\mathbf{r}}d^3\mathbf{r} = 1$ gives **Eqn. (1)** in the main text.

A3. The form factor

The form factor, $\sigma(\mathbf{r})$, describes the geometric boundary of an object possessing a different scattering strength than the surrounding medium. Making the fundamental assumption that the finite size of the particle has no statistical effect on the positions of the atoms within it, relative to an infinitely large object, then for a single finite particle:

$$p(\mathbf{r}) = \sigma(\mathbf{r})p_\infty(\mathbf{r}), \tag{A5}$$

where $p_\infty(\mathbf{r})$ describes a boundless region of material, and $\sigma(\mathbf{r}) = 1$ if $\mathbf{r}$ lies inside the particle, and zero otherwise. To understand the effect of a form factor upon the PDF, the relationship between $p(\mathbf{r})$ and $S(\mathbf{q})$ must be considered in more detail. Both $c(\mathbf{r})$ and $\rho(\mathbf{r})$ are related to the (Patterson) autocorrelation of $p(\mathbf{r})$.

$$c(\mathbf{r}) = \frac{1}{N} \int p(\mathbf{r}')p(\mathbf{r}'+\mathbf{r})d^3\mathbf{r}' \tag{A6}$$

The integrand is non-vanishing only when there is overlap between one or more atoms in the original structure and an identical copy displaced by $\mathbf{r}$. The introduction of the form factor $\sigma(\mathbf{r})$ via **Eqn. A5** has the effect of limiting the integration to the region of space common to the original particle and the notional copy (c.f. **Figure 2**). Then, for a single finite particle

$$c(\mathbf{r}) = \frac{1}{N} \int_{v(\mathbf{r})} p_\infty(\mathbf{r}')p_\infty(\mathbf{r}'+\mathbf{r})d^3\mathbf{r}' \tag{A7}$$

where $\upsilon(\mathbf{r}) = \int \sigma(\mathbf{r}')\sigma(\mathbf{r}'+\mathbf{r})d^3\mathbf{r}$ is the common volume within which the integration is performed. This term may also be written $\upsilon(\mathbf{r}) = Vf(\mathbf{r})$, where the shape factor, $f(\mathbf{r})$, is the *fractional* common volume at displacement $\mathbf{r}$. At zero displacement, $f(0) = 1$, because the integration is over the entire volume, V, of the single particle, while in general $0 < f(\mathbf{r}) \le 1$.

For a homogeneous material, with constant atom number density, the integral in Eqn. (20) is linearly proportional to the integration volume. This is a good approximation that becomes exact in the limit of infinite sample size:

$$\left(\int_{\upsilon(\mathbf{r})} p_\infty(\mathbf{r}')p_\infty(\mathbf{r}'+\mathbf{r})d^3\mathbf{r}'\right)\Big/\upsilon(\mathbf{r}) \approx \text{constant} = \lim_{\Omega\to\infty}\left[\left(\int_\Omega p_\infty(\mathbf{r}')p_\infty(\mathbf{r}'+\mathbf{r})d^3\mathbf{r}'\right)\Big/\Omega\right] \tag{A8}$$

and hence

$$c_\infty(\mathbf{r}) = \rho_o \lim_{\Omega\to\infty}\left[\left(\int_\Omega p_\infty(\mathbf{r}')p_\infty(\mathbf{r}'+\mathbf{r})d^3\mathbf{r}'\right)\Big/\Omega\right] \tag{A9}$$

This approach permits the definition of $c(\mathbf{r})$ for a simple particle to be rewritten:

$$\begin{aligned}
c(\mathbf{r}) &= \frac{\upsilon(\mathbf{r})}{N}\left(\int_{\upsilon(\mathbf{r})} p_\infty(\mathbf{r}')p_\infty(\mathbf{r}'+\mathbf{r})d^3\mathbf{r}'\right)\Big/\upsilon(\mathbf{r}) \\
&= \frac{Vf(\mathbf{r})}{N}\rho_o c_\infty(\mathbf{r}) \\
&= f(\mathbf{r})c_\infty(\mathbf{r})
\end{aligned} \tag{A10}$$

By noting that $\delta(\mathbf{r}) = 0$ for $\mathbf{r} \ne 0$, and that $f(0) = 1$, we can summarize the consequences of the form factor on the density correlation functions:

$$\rho(\mathbf{r}) \to f(\mathbf{r})\rho_\infty(\mathbf{r}) \tag{A11a}$$

$$c(\mathbf{r}) \to f(\mathbf{r})\rho_\infty(\mathbf{r}) + \delta(\mathbf{r}) \tag{A11b}$$

For a finite sample, following the approach in **§A2** with the substitution $\rho_\infty(\mathbf{r}) = \rho_o + \left[\rho_\infty(\mathbf{r}) - \rho_o\right]$ gives **Eqn. 7** in the main text.

Appendix B. Calculation of the shape factor of prolate and oblate spheroids.

As described in **§2.2.1**, the shape factor is directly calculated by considering the fractional common volume for a displacement of an object along a direction defined by the polar angle θ from the c axis. We apply the linear transformation $x \to (R/a)x$, $y \to (R/a)y$, $c \to (R/c)z$, shown in **Figure 2**. This transformation conserves the volume of the object while restoring it to a spherical morphology. The transformation does not affect the fractional common volume, which can then be found from the expression for a sphere with radius R and modified displacement, r'. Hence, the shape function for a spheroid is given by the integration

$$f_{spheroid}(r) = \int_{\theta_{\min}}^{\theta_{\max}} f_{sphere}(r',D)\sin\theta\,d\theta, \text{ where } D = 2R \text{ and} \tag{B1}$$

$$r'(\theta) = rR\sqrt{\sin^2\theta/a^2 + \cos^2\theta/c^2}. \tag{B2}$$

Setting $\eta = \sqrt{1-e^2}$, the shape factors for prolate and oblate spheroids are derived below.

B1. Prolate Spheroid

Substituting expressions for a and c:

$$r'(\theta) = \frac{r}{\sqrt{\eta}}\sqrt{1 - e^2\cos^2\theta} \tag{B3}$$

The limits of integration are set by considering whether the displaced objects touch for all angles.

For $0 < r < 2\sqrt{\eta}R$, the two objects interpenetrate at all angles, and $0 < \theta < \pi/2$:

$$f_{spheroid}^{prolate}(r,D) = 1 - \left(\frac{3}{2}\right)\left(\frac{r}{\sqrt{\eta}D}\right)\Gamma_1^{prolate}\left(e,\frac{\pi}{2}\right) + \left(\frac{1}{2}\right)\left(\frac{r}{\sqrt{\eta}D}\right)^3 \Gamma_2^{prolate}\left(e,\frac{\pi}{2}\right), \tag{B4}$$

where

$$\Gamma_1^{prolate}\left(e,\frac{\pi}{2}\right) = \frac{\sin^{-1}e}{2e} + \frac{\sqrt{1-e^2}}{2} \tag{B5a}$$

$$\Gamma_2^{prolate}\left(e,\frac{\pi}{2}\right) = \frac{3\sin^{-1}e}{8e} - \frac{\sqrt{1-e^2}}{8}\left(2e^2 - 5\right) \tag{B5b}$$

In the range $2\sqrt{\eta}R < r < 2R/\eta, \ 0 < \theta < \theta_{max}$, where $e^2\cos^2\theta_{max} = 1 - 4\eta R^2/r^2$:

$$f_{spheroid}^{prolate}(r,D) = \left(1 - \cos\theta_{max}\right) - \left(\frac{3}{2}\right)\left(\frac{r}{\sqrt{\eta}D}\right)\Gamma_1^{prolate}\left(e,\theta_{max}\right) + \left(\frac{1}{2}\right)\left(\frac{r}{\sqrt{\eta}D}\right)^3 \Gamma_2^{prolate}\left(e,\theta_{max}\right), \tag{B6}$$

where

$$\Gamma_1^{prolate}\left(e,\theta_{max}\right) = \frac{-\sin^{-1}\left(e\cos\theta_{max}\right)}{2e} - \frac{\cos\theta_{max}\sqrt{1 - e^2\cos^2\theta_{max}}}{2} \tag{B7a}$$

$$\Gamma_2^{prolate}\left(e,\theta_{max}\right) = \frac{-3\sin^{-1}\left(e\cos\theta_{max}\right)}{8e} + \frac{\cos\theta_{max}\sqrt{1 - e^2\cos^2\theta_{max}}}{8}\left(2e^2\cos^2\theta_{max} - 5\right) \tag{B7b}$$

B2. Oblate Spheroid

The modified interatomic distance can be expressed:

$$r'(\theta) = \frac{r}{\eta}\sqrt{1 - e^2 \sin^2 \theta} \tag{B8}$$

The limits of integration are set by the following ranges:

For $0 < r < 2\eta R, \ \ 0 < \theta < \pi/2$:

$$f_{spheroid}^{oblate}(r,D) = 1 - \left(\frac{3}{2}\right)\left(\frac{r}{\eta D}\right)\Gamma_1^{oblate}(e,0) + \left(\frac{1}{2}\right)\left(\frac{r}{\eta D}\right)^3 \Gamma_2^{oblate}(e,0), \tag{B9}$$

where

$$\Gamma_1^{oblate}(e,0) = \frac{1}{2} + \frac{(e-1)(e+1)}{2e}\left(\ln\left[\sqrt{2(1-e^2)}\right] - \ln\left[\sqrt{2}(e+1)\right]\right) \tag{B10a}$$

$$\Gamma_2^{oblate}(e,0) = \frac{(5-3e^2)}{8} + \frac{3(e^2-1)^2}{8e}\left(\ln\left[\sqrt{2}(e+1)\right] - \ln\left[\sqrt{2(1-e^2)}\right]\right) \tag{B10b}$$

For $2\eta R < r < 2R/\sqrt{\eta}, \ \ \theta_{min} < \theta < \pi/2$, where $e^2 \sin^2 \theta_{min} = 1 - 4\eta^2 R^2/r^2$

$$f_{spheroid}^{oblate}(r,D) = \cos\theta_{min} - \left(\frac{3}{2}\right)\left(\frac{r}{\eta D}\right)\Gamma_1^{oblate}(e,\theta_{min}) + \left(\frac{1}{2}\right)\left(\frac{r}{\eta D}\right)^3 \Gamma_2^{oblate}(e,\theta_{min}), \tag{B11}$$

where

$$\Gamma_1^{oblate}(e,\theta_{min}) = \frac{-\sqrt{2}}{4}\cos\theta_{min}\xi(e,\theta_{min}) + \frac{(e-1)(e+1)}{2e}\left(\ln\left[\sqrt{2(1-e^2)}\right] - \ln\left[\sqrt{2}e\cos\theta_{min} + \xi(e,\theta_{min})\right]\right) \tag{B12a}$$

$$\Gamma_2^{oblate}(e,\theta_{min}) = \frac{\sqrt{2}}{16}\cos\theta_{min}\xi(e,\theta_{min})\left(5 - 4e^2 + e^2\cos 2\theta_{min}\right)$$
$$+ \frac{3}{8}\frac{(e^2-1)^2}{e}\left(\ln\left[\sqrt{2}e\cos\theta_{min} + \xi(e,\theta_{min})\right] - \ln\left[\sqrt{2(1-e^2)}\right]\right) \tag{B12b}$$

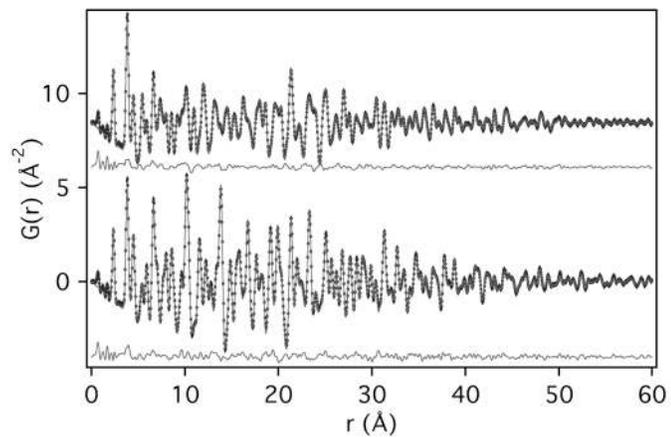and $\xi(e,\theta) = \sqrt{2 - e^2(1 - \cos 2\theta)}$.

Figure 1   Experimental (markers) and simulated (lines) pair distribution functions (PDF) of the common crystal phases of bulk zinc sulfide. Top: *hexagonal* wurtzite. Bottom: *cubic* sphalerite. The curves are displaced for clarity and the fit residuals are shown below. The decay of PDF intensity is due to the finite angular resolution at the image plate x-ray detector.
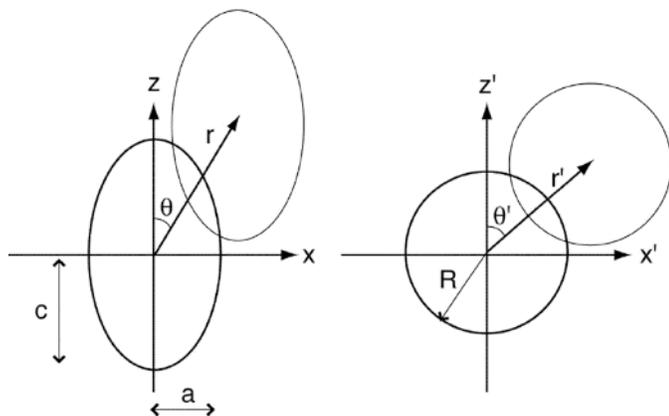
Figure 2 Method of calculation of the shape factor of a prolate spheroid. **Left**. The shape factor is proportional to the fractional volume, V', that is common to the spheroid and a copy displaced by **r**. **Right**. Calculation is aided by performing a linear transformation of the Cartesian axes that restores a spherical morphology.
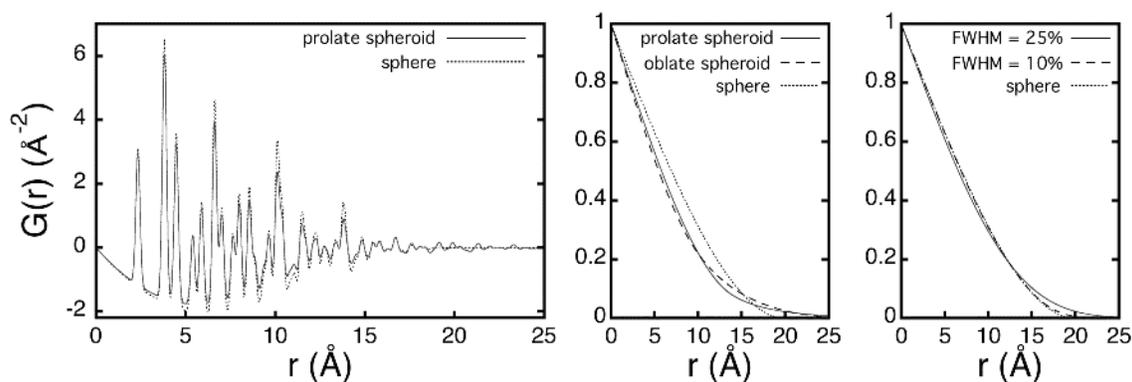

Figure 3 **a)** Simulated pair distribution functions for ZnS nanoparticles with the *cubic* sphalerite structure, either as 2 nm diameter spheres or prolate spheroids of equal volume and ellipticity, $e = 0.95$. **b)** Shape functions for a 2 nm diameter sphere, and prolate and oblate spheroids with equal volume and ellipticity, $e = 0.95$. **c)** Shape functions for a 2 nm diameter sphere and an ensemble of spheres with a normal distribution of radii.
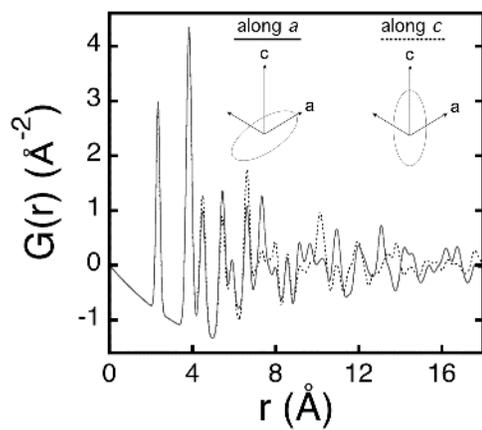
Figure 4   Simulated pair distribution functions for prolate spheroidal ZnS nanoparticles with the *hexagonal* wurtzite structure and ellipticity 0.99, for different orientations of the crystallographic axes relative to the particle shape. The nanoparticle volume is equivalent to a 3 nm diameter spherical particle.
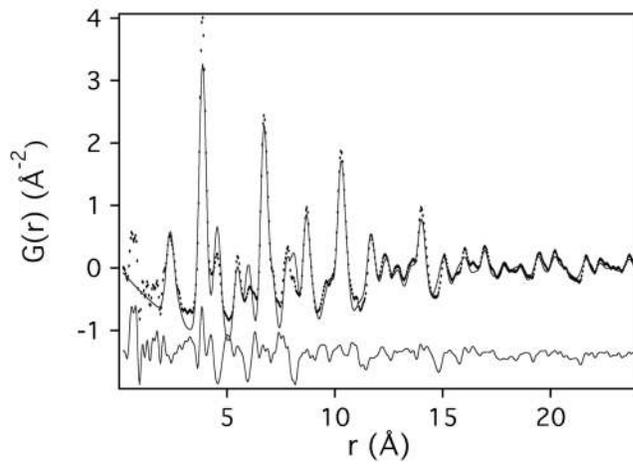
Figure 5 Experimental PDF of CeO₂ nanoparticles (markers) and best fit simulated PDF (line) using the fluorite structure with experimental and material parameters obtained from a fit to bulk CeO₂ (data not shown). The nanoparticle fit additionally includes a spheroidal shape factor, an isotropic lattice expansion, and thermal and structural disorder, as described in the text.
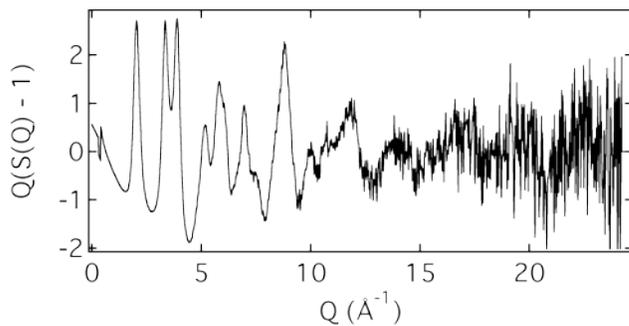
Figure 6 **a)** *Q*-weighted structure factor for 3 nm diameter aggregated, uncoated ZnS nanoparticles. **b)** Experimental PDF and best fit simulated PDF for 3 nm ZnS nanoparticles. The fitted PDF assumes a cubic ZnS structure with correlated thermal disorder obtained from a fit to bulk *cubic* ZnS, 3 nm spherical morphology plus additional structural harmonic disorder and short-range order function. Data = markers; fit = grey line; residuals below. **c)** Contributions to PDF peak width broadening: thermal (grey dotted line) and static (solid line) disorder. The thermal contribution was obtained from the fit to bulk *cubic* ZnS given in **Figure 1**. **d)** Contributions to PDF peak intensity reduction: shape factor for 3 nm diameter sphere (grey dotted line) and empirical "short-range order" scaling factor (solid line).